

Size-dependence of Fermi energy of gold nanoparticles loaded on titanium(IV) dioxide at photostationary state

Tomokazu Kiyonaga,^a Masashi Fujii,^a Tomoki Akita,^b Hisayoshi Kobayashi^c and Hiroaki Tada^{*a}

Received 9th June 2008, Accepted 31st July 2008

First published as an Advance Article on the web 24th September 2008

DOI: 10.1039/b809681c

TiO₂ particle-supported Au nanoparticles (NPs) with varying sizes and good contact (Au/TiO₂) were prepared under a constant loading amount by the deposition-precipitation method. The Fermi energy of Au NPs loaded on TiO₂ at the photostationary state (E_F') was determined in water by the use of S/S²⁻ having specific interaction with Au as a redox probe. The E_F' value goes up as the mean size of Au NPs (d) increases at $3.0 \leq d \leq 13$ nm. The photocatalytic activities for the Au/TiO₂-photocatalyzed reductions of 2,2'-dipyridyl disulfide and nitrobenzene increase with increasing d . The photoluminescence spectra for Au/TiO₂ and their dynamic analysis indicated that the efficiency of the interfacial electron transfer from TiO₂ to Au NPs increases as the result of an increase in d . Density functional theoretical calculations for (Au)₁₀ and (Au)₂₂ model clusters showed that negatively charged Au clusters are greatly stabilized by water solvation, of which energy is smaller for (Au)₂₂. The d -dependence of E_F' could be rationalized in terms of both the increase in the efficiency of the photoinduced electron transfer and the strong solvation of charged Au NPs by water. The parallel correlation between the E_F' and photocatalytic activity proves for E_F' to be a very important parameter for designing metal NP-loaded semiconductor photocatalysts.

1. Introduction

The development of green processes for decomposing harmful compounds and producing useful ones are crucial subjects imposed on chemistry. On the premise that sunlight or illuminating light is used as a light source, semiconductor-photocatalyzed reactions can be a promising approach to achieve them. It is well known that the photocatalytic activity significantly increases with loading nanometer-sized noble metal particles.^{1,2} Essentially, this results from the increase in the charge separation efficiency due to the interfacial electron transfer from semiconductors to metals.^{3,4} Among the semiconductor photocatalysts, much attention has so far been focused on TiO₂ because of its strong oxidation power of the holes photogenerated in the valence band (v.b.) to oxidize most toxic organic compounds.⁵ Recently, the loading of Au nanoparticles (NPs) on mesoporous TiO₂ has been shown to enhance the photocatalytic activity for the decomposition of phenol.⁶ On the other hand, the applications to organic synthesis are highly expected by taking advantage of the mild reducing power of the excited electrons in the conduction band (c.b.).⁷ We have reported the drastic enhancement of the TiO₂-photocatalyzed reductions of disulfides^{8,9} and nitrobenzene¹⁰ with loading Au and Ag NPs on TiO₂ (Au/TiO₂ and Ag/TiO₂).

These are good examples of the so-called “reasonable delivery photocatalytic reactions systems (RDPRS)”,¹¹ which satisfy the following three conditions for effecting high efficiency and selectivity: (i) separation of oxidation and reduction sites; (ii) abundant and selective supply of oxidants and reductants to reduction sites (metal surface) and oxidation sites (TiO₂ surface), respectively; and (iii) restriction of the product readsorption. In this case, if the Fermi energy of the metal NPs loaded on TiO₂ at the photostationary state (E_F') can be determined, it should be very useful to design photocatalytic organic synthesis. Since the E_F' dictates the photovoltage in dye-sensitized solar cells (DSSC), it is of great importance also in DSSC.¹² In the pioneering work on *n*-TiO₂ electrodes covered with discontinuous Au films, Nakato *et al.* showed that the photopotential of *n*-TiO₂ is not in agreement with that of Au, while both the potentials shift cathodically.¹³ This study provides important information about the action mechanism of the metal loading on semiconductor photocatalysts. However, most of the photocatalytic reactions were carried out in particulate systems. Recently, the research group of Kamat has determined the Fermi energy of irradiated Au/TiO₂ particles in organic solvent using a C₆₀/C₆₀⁻ redox pair.¹⁴ Hereafter, organic synthesis using water as a green solvent will increasingly become important from a viewpoint of environmental conservation. To our knowledge, the method for determining E_F' in water has not yet been presented.

In this study, the E_F' value of Au/TiO₂ in water has been determined using a S/S²⁻ redox pair having a specific interaction with Au NPs.¹⁵ Further, the Au particle-size dependences of the E_F' and photocatalytic activity of Au/TiO₂ were examined, and the correlation was discussed

^a Department of Applied Chemistry, School of Science and Engineering, Kinki University, 3-4-1, Kowakae, Higashi-Osaka, Osaka, 577-8502, Japan. E-mail: h-tada@apch.kindai.ac.jp; Fax: + 81-6-6727-2024; Tel: + 81-6-6721-2332

^b National Institute of Advanced Industrial Science and Technology, Midorigaoka 1-8-31, Ikeda, Osaka, 563-8577, Japan

^c Department of Chemistry and Materials Technology, Kyoto Institute of Technology, Matsugasaki, Sakyo-ku, Kyoto, 606-8585, Japan

based on the experimental and density functional theoretical (DFT) calculation results.

2. Experimental

2.1 Materials and characterization

Au particles were loaded on TiO₂ particles with a crystal form of anatase and a specific surface area of 8.1 m² g⁻¹ (A-100, Ishihara Sangyo) by the deposition-precipitation (DP) method using HAuCl₄ as a raw material.¹⁶ The specific surface areas of the metal oxides and the mean diameters of the metal clusters (*d*) were determined by the Brunauer–Emmett–Teller method and transmission electron microscopy at an applied voltage of 300 kV (JEM-3010, JEOL), respectively. The amounts of the metal clusters were quantified by inductively coupled plasma spectroscopy (ICPS-7500, Shimadzu). The surface areas of the metal clusters were calculated from their amounts and *d* values.

2.2 Photoinduced sulfur desorption

Prior to the sulfur desorption experiments, sulfur was adsorbed on Au/TiO₂ by adding the particles (3.0 g) to an 0.97 mmol dm⁻³ S₈ solution (0.5 L) and stirring for 24 h at 298 K. The particles were then separated from the solution by centrifugation, washed with water three times, and dried in vacuum (S–Au/TiO₂). After the aqueous suspension of S–Au/TiO₂ had been purged with argon for 15 min, irradiation was started using a high-pressure mercury lamp (H-400P, Toshiba) in a double jacket-type reaction cell (31 mm in diameter and 175 mm in length, transparent to light with $\lambda > 300$ nm). Since S₈ hardly absorbs light of $\lambda > 300$ nm, Au/TiO₂ is almost selectively excited under the conditions. The pH value of the suspension was controlled at 13 by adding 0.02 mol dm⁻³ NaOH solutions. The light intensity integrated from 310 to 400 nm (*I*_{310–400}) was measured to be 4.0 mW cm⁻² by the use of a digital radiometer (UM-360, Konica Minolta). The temperature of the suspension was kept at 298 K by circulating thermostatted water through an outer jacket around the cell. After the sulfurs adsorbed on Au/TiO₂ before and after irradiation (0.25 g) had been completely oxidized to SO₄²⁻ ions by adding a 16% H₂O₂ solution and 1.15 × 10⁻³ mol dm⁻³ phosphoric acid (30 mL) and stirring for 16 h, they were quantified by ion chromatography (PIA-1000, Shimadzu). In this analysis, a mixed solvent consisting of 12 mmol dm⁻³ *p*-hydroxybenzoic acid and 4.0 mmol dm⁻³ 2,2-bis(hydroxymethyl)-2,2',2''-nitrilotriethanol were used as a mobile phase.

2.3 Photocatalytic reactions

The photoreaction solution of 5.4 × 10⁻⁵ mol dm⁻³ 2,2'-dipyridyl disulfide (RSSR) was prepared by diluting an acetonitrile solution with H₂O (H₂O:acetonitrile = 99:1 v/v). After the suspension (50 mL) of TiO₂ or Au/TiO₂ (50 mg) had been purged with Ar for 15 min, irradiation was started using a high-pressure mercury lamp (H-400P, Toshiba) in a double jacket type reaction cell (31 mm in diameter and 175 mm in length, transparent to light with $\lambda > 300$ nm). The light intensity integrated from 310 to 400 nm (*I*_{310–400}) was measured to be 4.0 mW cm⁻² by the use of a digital radiometer (UM-360, Konica Minolta). Ar bubbling and magnetic stirring of the suspension were continued throughout the irradiation. The

temperature of the suspension was kept at 298 K by circulating thermostatted water through an outer jacket around the cell. The concentrations of RSSR consumed and 2-mercaptopyridine (RSH) generated were determined from the absorbances at 281 nm ($\epsilon_{\text{max}} = 1.05 \times 10^4 \text{ mol}^{-1} \text{ dm}^3 \text{ cm}^{-1}$) and 342 nm ($\epsilon_{\text{max}} = 7.18 \times 10^3 \text{ mol}^{-1} \text{ dm}^3 \text{ cm}^{-1}$), respectively.

TiO₂ or Au/TiO₂ particles (50 mg) were added to a 1.1 × 10⁻³ mol dm⁻³ nitrobenzene (NB) solution (50 mL, solvent = H₂O:acetonitrile = 99:1 v/v). The suspension was bubbled with argon for 20 min in the dark (pH 6.8), and then irradiation ($\lambda > 300$ nm) started using a high-pressure mercury lamp (H-400P, Toshiba): the light intensity integrated from 310 to 400 nm was measured to be 4.0 mW cm⁻². The argon bubbling was continued throughout the reaction. The cell was kept at 298 K by circulating thermostatted water through an outer jacket around the cell. For the quantification of the reactant and product, the irradiated solution was analyzed by high-performance liquid chromatography (LC-6AD, SPD-6A, C-R8A (Shimadzu)) [measurement conditions: column = Shim-pack CLC-ODS 4.6 × 150 mm; mobile phase H₂O–CH₃OH (3/7 v/v); flow rate = 0.5 mL min⁻¹; $\lambda = 270$ nm].

2.4 Electronic absorption and photoluminescence (PL) spectroscopic measurements

The electronic absorption spectra of TiO₂ and Au/TiO₂ particles with varying *d* values were recorded by the diffuse reflectance method using an integral sphere on a Hitachi U-4000 spectrophotometer at a scan speed of 60 nm min⁻¹ in the 300–800 nm range. The PL spectra of TiO₂ and Au/TiO₂ particles were measured with an excitation wavelength of 300 or 340 nm at room temperature or 77 K using a JASCO FP-6500 spectrofluorometer.

2.5 DFT calculations

A computer simulation based on the DFT method was carried out using the Gaussian 98 program.¹⁷ The hybrid Becke–three-parameter–Lee–Yang–Parr functional was adopted,^{18,19} which includes the gradient corrected exchange²⁰ and correlation functionals²¹ together with the local functionals and the Hartree–Fock exchange operator. The Los Alamos effective core potential and the corresponding valence basis set were used for Au.^{22,23} The solvation effects of water molecules were considered by the polarized continuum model (PCM) in the framework of self-consistent reaction field (SCRF) theory.²⁴ (Au)₁₀ and (Au)₂₂ clusters were truncated from the (111) surface, and model the corner sites of micro particles. The total energies were evaluated for the charges of +1 to –10 and +1 to –11 for (Au)₁₀ and (Au)₂₂, respectively, in vacuum and in water (with the PCM).

3. Results and discussion

3.1 Characterization of Au/TiO₂

Generally, the photocatalytic activity of metal-loaded semiconductor photocatalysts depends on the metal loading amount.^{25,26} In order to examine the metal particle-size dependence of the photocatalytic activity, therefore, it is necessary to vary the metal particle size with its loading

amount maintained constant. For this purpose, Au NPs were incorporated on TiO₂ by the deposition–precipitation method where both heating temperature (T_c) and time (t_c) were altered.²⁷ Notice here that changing T_c causes the variation in the crystallinity and the number of oxygen-vacancy of TiO₂ to affect its photocatalytic activity. Hence, all the TiO₂ particles were heated at 923 K for 4 h prior to the use for the preparation of Au/TiO₂, which allows us to neglect the changes of TiO₂ with different T_c below 873 K. Fig. 1 shows TEM images (left) and Au particle size distribution (right) of Au/TiO₂ prepared under different heating conditions: (A) $T_c = 673$ K, $t_c = 1$ h; (B) $T_c = 673$ K, $t_c = 4$ h; (C) $T_c = 873$ K, $t_c = 4$ h. In every sample, Au NPs highly dispersed on the TiO₂ surface have a fairly sharp distribution. The mean size of Au NPs (d) increases from 4.2 to 13 nm as a result of an increase in T_c from 673 to 873 K, while the loading amount remains almost constant (0.43–0.46 mass%). To check the state of the Au–TiO₂ junction, Au NPs loaded on a TiO₂ single crystal were observed by high-resolution TEM (HRTEM). Fig. 1D is a typical HRTEM image of Au NP (0.44 mass%). The Au particle is supported on the TiO₂{101} surface with an orientation relationship of Au{111}//TiO₂{101}. Most Au NPs are single crystals with the fcc structure surrounded by the low index (111) and (100) planes, as predicted by the Wulff construction. The truncated shape Au particle is in good contact with TiO₂ at an atomic level, having a large interfacial area because of the low interfacial energy between Au and TiO₂. Large (111) facets with the smallest surface energy in the fcc crystal structure are usually observed. Thus, Au NPs with varying sizes and good contact can be formed on the TiO₂ surface under a constant loading amount by this DP method.

3.2 Adsorption and photoinduced desorption of sulfur on/from Au/TiO₂

The Au NP-loading effect on the adsorption properties of elemental sulfur (S₈) was examined. Fig. 2A shows the adsorption isotherms of S₈ from ethanol solutions on TiO₂ (a) and Au($d = 3.2$ nm)/TiO₂ (b) at 298 K. A drastic increase in the adsorption amount of S₈ is observed as a result of such a small amount loading of Au. The adsorption selectivity defined as $n_s(\text{Au})/\{n_s(\text{TiO}_2) + n_s(\text{Au})\}$ reaches as much as 99.6%, where $n_s(\text{Au})$ and $n_s(\text{TiO}_2)$ are the saturated adsorption amounts on the Au and TiO₂ surfaces, respectively. Evidently, S₈ is highly selectively adsorbed on the Au(111) surfaces of Au NPs. Upon irradiation to the Au/TiO₂ in a saturated adsorption state (S–Au/TiO₂), part of the sulfur is efficiently reduced to S^{2–} to be desorbed into water at room temperature.¹⁵ The ratio of sulfur desorbed from S–Au/TiO₂ dispersed in water was measured for the samples having different d values. Fig. 2B shows the sulfur desorption ratio ($X = \text{desorbed sulfur}/\text{initially adsorbed sulfur}$) as a function of irradiation time (t_p). In every sample, the X value abruptly increases on irradiation, reaching a constant value at $t_p > 20$ min. When the suspension containing 0.2 vol% TiO₂ particles was irradiated from the upper side of the reaction vessel, light absorption by TiO₂ particles is limited to approximately 1 mm of the suspension because the absorption coefficient of TiO₂ in the UV region is about 10^4 cm^{-1} .²⁸ Since Au/TiO₂ particles are

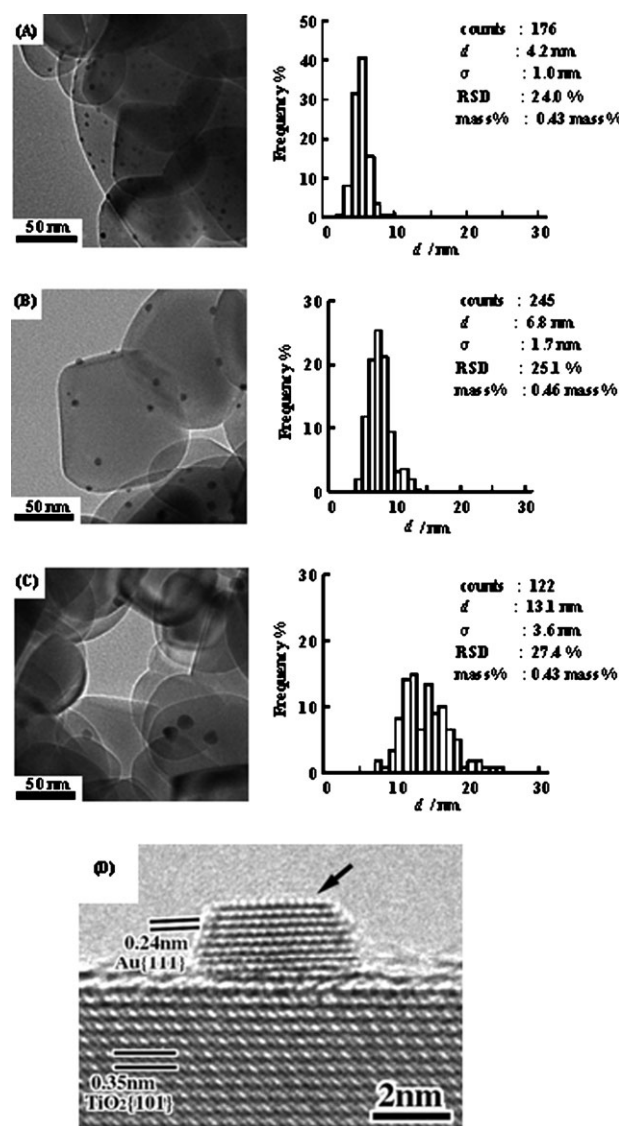


Fig. 1 TEM images of Au/TiO₂ particles prepared under various heating conditions (left) and their size distribution of the Au particles (right): (A) $T_c = 673$ K, $t_c = 1$ h; (B) $T_c = 673$ K, $t_c = 4$ h; (C) $T_c = 873$ K, $t_c = 4$ h, and an HRTEM image of a Au nanoparticle loaded on TiO₂ (D).

continuously moving throughout the reaction vessel due to stirring and convection under the present conditions, part of the sulfur desorbed as S^{2–} ions would be readsorbed on the Au surfaces of Au/TiO₂, below this region.²⁹ Assuming that the rates of sulfur desorption and readsorption are equal at the photo-stationary state, one can obtain eqn (1) relating X to t_p .³⁰

$$X(t_p) = [k_d/(k_a + k_d)][1 - \exp\{-(k_a + k_d)t_p\}] \quad (1)$$

where k_d and k_a express the rate constants of sulfur desorption and readsorption, respectively.

As shown in Fig. 2B, the theoretical curves calculated by the least square method with eqn (1) fit well with the experimental data. The saturated desorption ratio (X_s) given by $k_d/(k_a + k_d)$ increases with increasing d . A similar trend was observed also for the Pt NP-loaded TiO₂ particle system at $1.1 \leq d \leq 9.2$ nm.³¹

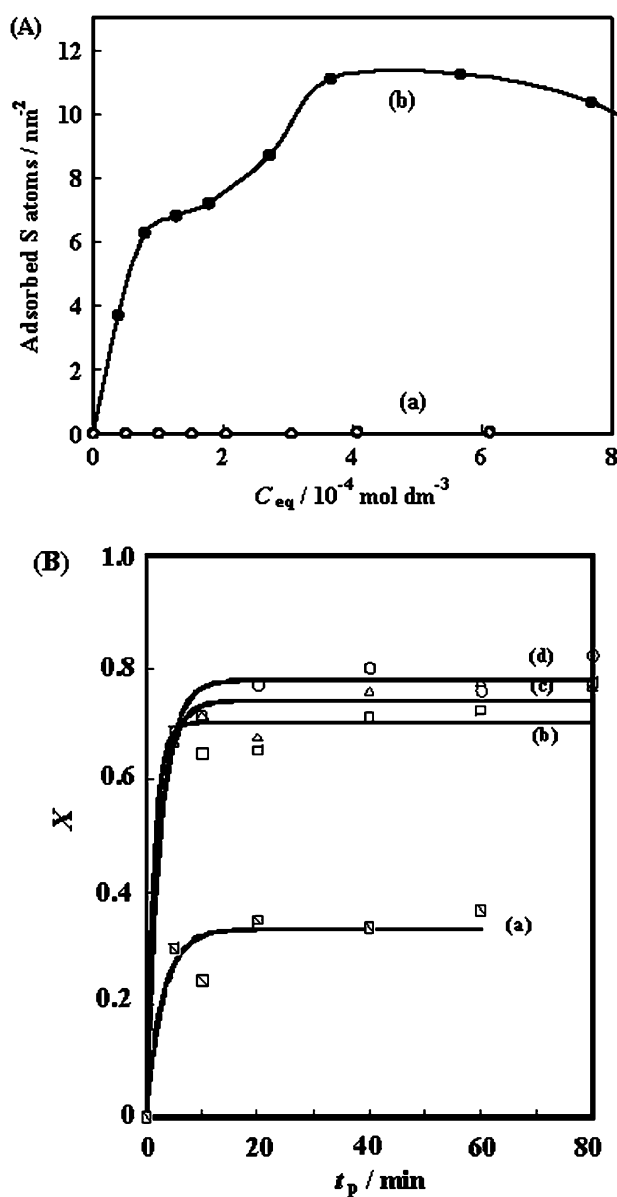


Fig. 2 (A) Adsorption isotherms of S₈ on TiO₂ (a) and Au/TiO₂ (b) at 298 K. (B) Time courses for the photoinduced sulfur desorption from S-Au/TiO₂: (a) $d = 4.2$ nm, (b) $d = 6.8$ nm, (c) $d = 8.1$ nm, (d) $d = 12$ nm.

3.3 Determination of E_F'

Redox properties of S²⁻ ions on Au NP-loaded TiO₂ films formed on F doped-SnO₂ electrodes (Au/TiO₂/SnO₂) were studied to specify the adsorption state of S²⁻ ions on the Au NP surfaces of Au/TiO₂ using cyclic voltammetry. Fig. 3A shows cyclic voltammograms of TiO₂/SnO₂ (a) and Au/TiO₂/SnO₂ (b) in a 0.5 mmol dm⁻³ Na₂S solution containing 0.1 mol dm⁻³ NaClO₄. Two pairs of redox waves are observed for Au/TiO₂/SnO₂ (curves (b) and (c)), whereas TiO₂/SnO₂ is almost inactive in the potentials (U/V vs. Ag/AgCl) ranging from -1.0 to +0.3 V (curve (a)). Apparently, the Au NPs act as a good electrocatalyst for the redox reactions of sulfur. When the potential is scanned from the rest potential (-0.50 V) toward the anodic direction first (curve (b)), an oxidation wave appears at -0.11 V corresponding to the

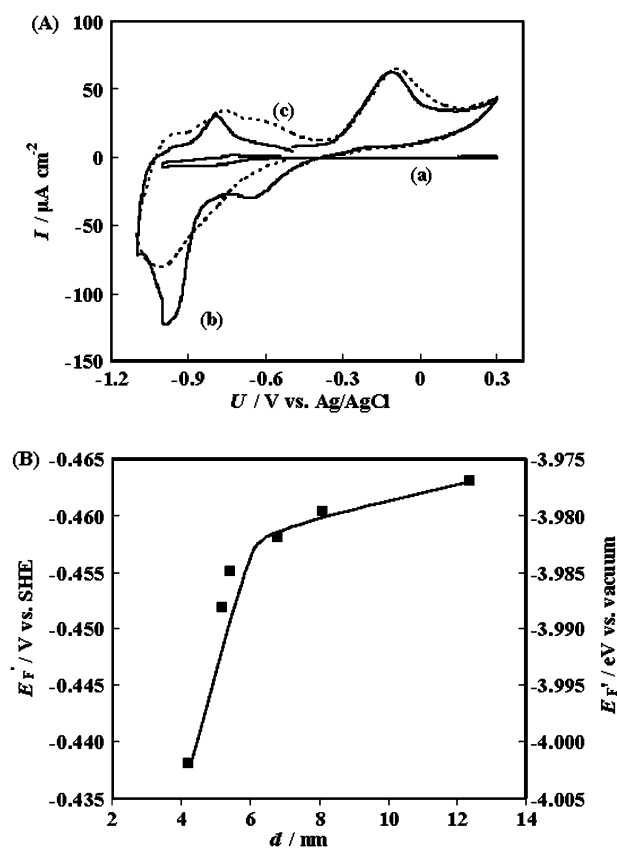
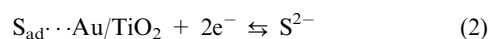


Fig. 3 (A) Cyclic voltammograms of TiO₂/SnO₂ (a) and Au/TiO₂/SnO₂ for starting from anodic (b) and cathodic (c) scan in a 0.5 mmol dm⁻³ Na₂S solution containing 0.1 mol dm⁻³ NaClO₄ as a supporting electrolyte. (B) Plots of E_F' vs. d at pH 13: light intensity integrated from 310 to 400 nm ($I_{310-400}$) = 4.0 mW cm⁻².

formation of S-multilayers.³² On reversing the sweep direction (curve (c)), only a reduction wave corresponding to the reduction of S to S²⁻ ions is observed at -1.0 V³³ with the absence of the reduction peak at -0.66 V due to the reduction of S-multilayers to S (see curve (b)). These results clearly indicate that S²⁻ ions are adsorbed on the Au NP surfaces as S in the dark, which was previously confirmed by X-ray photoelectron spectroscopy.³⁴ Thus, the present reaction at the photostationary state can be expressed by eqn (2).



The application of Nernst's equation to eqn (2) yields eqn (3) relating E_F' to X_s . It should be noted here that E_F' provides the Fermi energy of Au NPs loaded on TiO₂ because sulfur is selectively adsorbed (and desorbed) on (and from) the Au NP surface.

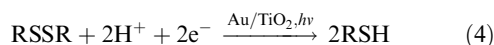
$$E_F' = E_0 + (RT/2F)\ln[(1 - X_s)/X_s] \quad (3)$$

where E_0 is the standard redox potential of S/S²⁻ (-0.447 V vs. SHE).³⁵

Fig. 3B shows E_F' calculated from eqn (3) (left axis) and scaled from vacuum level (right axis) as a function of d . Interestingly, E_F' rises as the d value increases at $3.0 \leq d \leq 13$ nm. Note here that the E_F' value should also depend on the irradiation conditions, *i.e.*, the light wavelength and intensity.

3.4 Au particle-size dependence of the photocatalytic activity of Au/TiO₂

As a first test reaction, the Au/TiO₂-photocatalyzed reduction of RSSR to RSH, a typical RDPRS, was carried out.⁹ Fig. 4A shows the electronic absorption spectral change of the reaction solutions under UV-light irradiation in the presence of Au/TiO₂. With irradiation, a new absorption centered at 342 nm of RSH appears, while the absorption band with a peak at 233 nm of RSSR weakens. Also, the presence of isosbestic points at 218, 247, and 295 nm indicates that this reaction almost selectively proceeds (eqn (4)).



Further, Au particle-size effect on the photocatalytic activity for the RSSR reduction was studied. Fig. 4B shows plots of the initial rate of reaction (v_0) vs. d , where the v_0 value for $d = 0$ expresses that for the TiO₂ system. The photocatalytic activity significantly increases as a result of the Au NP loading. The v_0 value increases with increasing d in spite of the decrease in the Au surface area.

Au/TiO₂-photocatalyzed reduction of nitrobenzene (NB) also belonging to RDPRS was performed as a second test reaction.¹⁰ The addition of CH₃OH as a hole scavenger causes the NB reduction to proceed, whereas no reduction occurred in water for both the TiO₂ and Au/TiO₂ systems. Fig. 4C shows electronic absorption spectral change of the reaction solution with UV-light irradiation in the presence of Au/TiO₂: [CH₃OH] = 100 mmol dm⁻³. Irradiation yields a new absorption around 230 nm due to aniline (AN), accompanied by a decrease in the

absorption of NB centered at 270 nm. Since isosbestic points are situated at 210 nm, 220 nm and 245 nm, the 6-electron reduction of NB to AN proceeds almost selectively (eqn (5)).

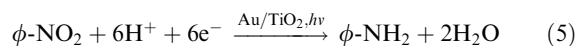


Fig. 4D shows the turnover frequency (TOF) for the Au/TiO₂-photocatalyzed reduction of NB as a function of d ($3.0 < d < 13$ nm): [CH₃OH] = 100 mmol dm⁻³. On the assumption that the surface Au atom is the reduction site, the TOF was calculated from the loading amount and d value. Au NP-loading gives rise to a drastic increase in the photocatalytic activity, whereas no reduction occurs without Au NPs ($d = 0$). Also, the TOF increases as the d value increases. The profiles of the d -dependences of the photocatalytic activities (Fig. 4B and D) well resemble that of the E_F' vs. d plots (Fig. 3B). Thus, the increase in the activity for the Au/TiO₂-photocatalyzed reduction with increasing d can be attributed to the increase in E_F' , i.e., the increase in the electronic potential of Au NPs coupled with TiO₂.

3.5 Au particle-size dependence of the photoluminescence intensity of Au/TiO₂

Photoluminescence (PL) measurements provide valuable information on the interfacial electron transfer in the metal-semiconductor coupled systems.³⁶ Fig. 5A shows electronic absorption spectra (left) and PL spectra (right) with an excitation wavelength of 300 nm at room temperature for TiO₂ (a, a'), Au($d = 4.2$ nm)/TiO₂ (b, b'), and Au($d = 13$ nm)/TiO₂ (c, c'). In the absorption spectra, Au/TiO₂ has a broad absorption around 550 nm due to

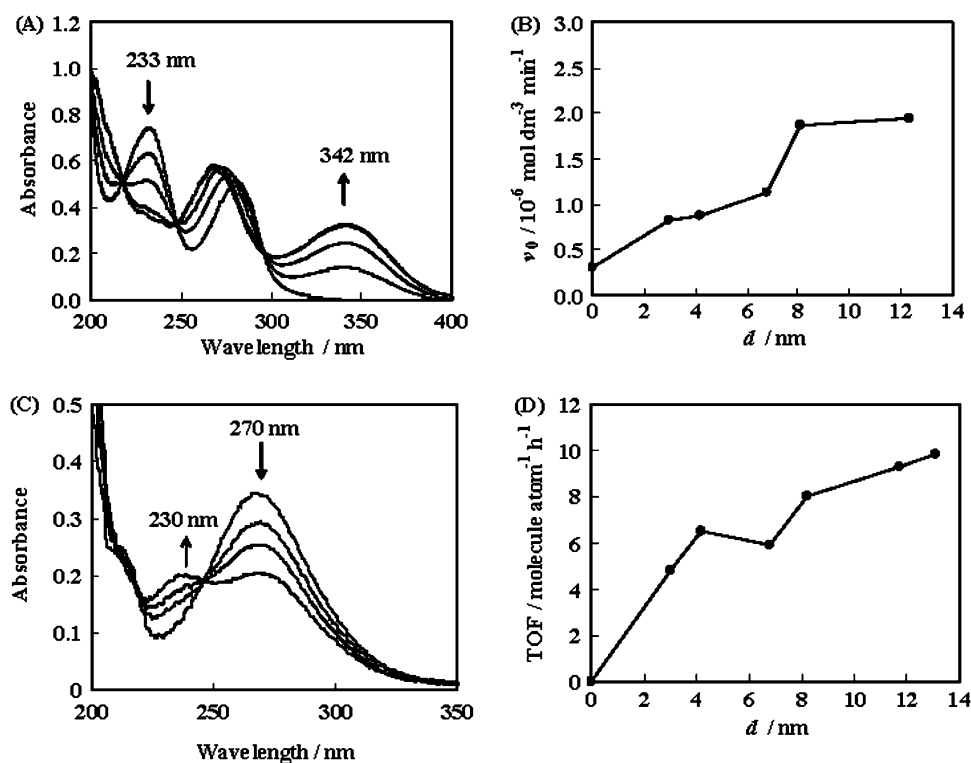


Fig. 4 (A) Electronic absorption spectral change of a $5.4 \times 10^{-5} \text{ mol dm}^{-3}$ RSSR solution with irradiation ($\lambda > 300 \text{ nm}$, $I_{310-400} = 4.0 \text{ mW cm}^{-2}$). (B) Plots of v_0 vs. d for the Au/TiO₂-photocatalyzed RSSR reduction. (C) Electronic absorption spectral change of a $1.1 \times 10^{-3} \text{ mol dm}^{-3}$ NB solution with irradiation ($\lambda > 300 \text{ nm}$, $I_{310-400} = 4.0 \text{ mW cm}^{-2}$). (D) Plots of TOF vs. d for the Au/TiO₂-photocatalyzed NB reduction.

the surface plasmon resonance of Au NPs along with a strong absorption band below 385 nm due to the interband transition of TiO₂. Also, the intensity of the Au surface plasmon band for Au(*d* = 13 nm)/TiO₂ is greater than that for Au(*d* = 4.2 nm)/TiO₂.³⁷ On the other hand, in the PL spectrum of TiO₂, a broad emission band is present in the range from 380 to 700 nm. The main band at 424 nm (B₁) can be assigned to the band-band PL. Also, a sharp band at 470 nm (B₂) is attributed to the emission from (oxygen) vacancy levels. Further, a band at 575 nm (B₃) may result from impurity levels because pure TiO₂ does not have this PL band.³⁸ There are two kinds of electron-trap sites in the TiO₂ particles used in this study. When Au NPs are loaded on TiO₂, the relative PL intensity decreases, although the spectral profile is invariant. A similar trend has recently been reported also for the Ag/TiO₂ particles.³⁹ Interestingly, the decreasing degree of the PL intensity for Au(*d* = 13 nm)/TiO₂ is greater than that for Au(*d* = 4.2 nm)/TiO₂. The PL intensity is thought to decrease with the Au-NP loading because of the reduction in the recombination due to the interfacial electron transfer from TiO₂ to Au. Further, the efficiency of the interfacial electron transfer is suggested to increase as the *d* value increases in the range below 13 nm.

Fig. 5B shows PL intensity at 530 nm (*I*) vs. time curves for TiO₂ (a), Au(*d* = 4.2 nm)/TiO₂ (b), and Au(*d* = 13 nm)/TiO₂ (c) with an excitation wavelength of 340 nm at 77 K. Each data can be well fitted by a double-exponential function (eqn (6)), and Table 1 summarizes the fitting parameters.

$$I(t) = c_1 \exp(-t/\tau_1) + c_2 \exp(-t/\tau_2) \quad (6)$$

where *c*₁ (*c*₂) and *τ*₁ (*τ*₂) are the weight and life-time of the longer-life (the shorter-life) component, respectively.

As a result of Au-NP loading on TiO₂, two significant changes are apparent. One is the increase in the ratio of *c*₂ to *c*₁, and another is the decreases in *τ*₁ and *τ*₂. Also, these tendencies are more pronounced in Au(*d* = 13 nm)/TiO₂. Fig. 5C shows delayed PL spectra of TiO₂ (a), Au(*d* = 4.2 nm)/TiO₂ (b), and Au(*d* = 13 nm)/TiO₂ (c) with an excitation wavelength of 340 nm; delayed time = 25 ms. Each spectrum has a broad PL band at *λ* > 450 nm, of which peak position is close to that of B₃ in Fig. 5A. The direct electron-hole recombination is a ultrafast event occurring at times 1 ps.⁴⁰ Accordingly, B₂ and B₃ are tentatively assignable to the shorter-life PL from shallow trap sites at *ca.* 0.6 eV below the c.b. and the longer-life PL from deep trap sites at *ca.* 1.0 eV below the c.b., respectively. A new path of the excited electron transfer from TiO₂ to Au explains the decrease in the PL life time with the Au-NP loading. In this manner, the conclusion can be drawn also from the kinetic analysis of the PL spectra that the efficiency of the interfacial electron transfer from TiO₂ to Au increases as the *d* value increases. This is further consistent with the experimental results that the *E*_F' value increases to improve the photocatalytic activity for the Au/TiO₂-photocatalyzed reduction with increasing *d*.

3.6 Theoretical considerations to the Au particle-size dependence of *E*_F' for Au/TiO₂

Downsizing the metal particle at a given loading amount necessarily increases its number density. It was previously

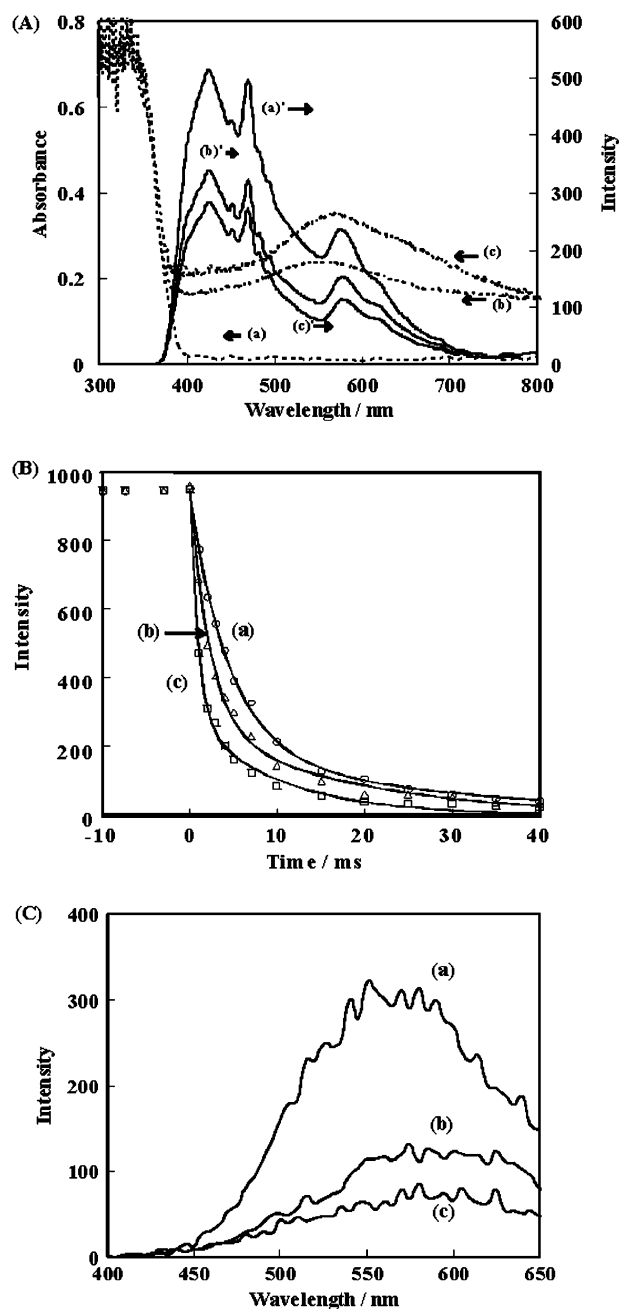


Fig. 5 (A) Electronic absorption spectra (left) and PL spectra (right) of TiO₂ (a), Au(*d* = 4.2 nm)/TiO₂ (b) and Au(*d* = 13 nm)/TiO₂ (c); measurement temperature = 298 K. (B) Decay curves of PL at 530 nm TiO₂ (a), Au(*d* = 4.2 nm)/TiO₂ (b) and Au(*d* = 13 nm)/TiO₂ (c); measurement temperature = 77 K. (C) Delayed PL spectra of TiO₂ (a), Au(*d* = 4.2 nm)/TiO₂ (b) and Au(*d* = 13 nm)/TiO₂ (c) measured at 77 K; delay time = 25 ms, measurement temperature = 77 K.

Table 1 Kinetic parameters for the decay of excited TiO₂ and Au/TiO₂

	TiO ₂	Au(4.2 nm)/TiO ₂	Au(13.1 nm)/TiO ₂
<i>c</i> ₁	737	680	664
<i>τ</i> ₁ /ms	4.43	2.27	0.93
<i>c</i> ₂	199	267	282
<i>τ</i> ₂ /ms	26.5	17.6	10.0

shown by dissolving 2D-Poisson's equation for metal particle-loaded TiO₂ that the metal NPs produce the electric field at the metal/TiO₂ interface to enhance the charge separation.^{41,42} However, when too many metal particles are loaded on a single TiO₂ particle, the charge separation effect is rather vitiated due to the overlap of the interfacial electric field. This reasonably explains the conclusion drawn from the PL measurements that the efficiency of the interfacial electron transfer from TiO₂ to Au NPs increases with increasing d at $3.0 \leq d \leq 13$ nm.

In order to obtain general understanding of the d -dependence of E_F' , the chemical potential (μ) for model Au clusters was calculated from eqn (7) by the DFT calculations as a function of excess electron number n .

$$\mu = -(I_p + E_A)/2 \quad (7)$$

where I_p and E_A are ionization potential and electron affinity, respectively.

The value of μ can be compared to the E_F' value experimentally determined. Fig. 6 shows the structures of the model clusters ((Au)₁₀ (a) and (Au)₂₂ (b)) used for the calculations, which were truncated from the Au(111) plane. The Au₁₀ cluster is frequently used for theoretical studies of adsorption of simple molecules to fcc(111) surface, such as Ni, Cu, Pd, Ag, Pt, and Au. In those cases, the Au₇ hexagon represents the (111) surface, and the three Au atoms for the second layer. In this study, since the reaction on the Au NP surface possibly occurs at some defect sites (kink or corner sites) on the surface rather

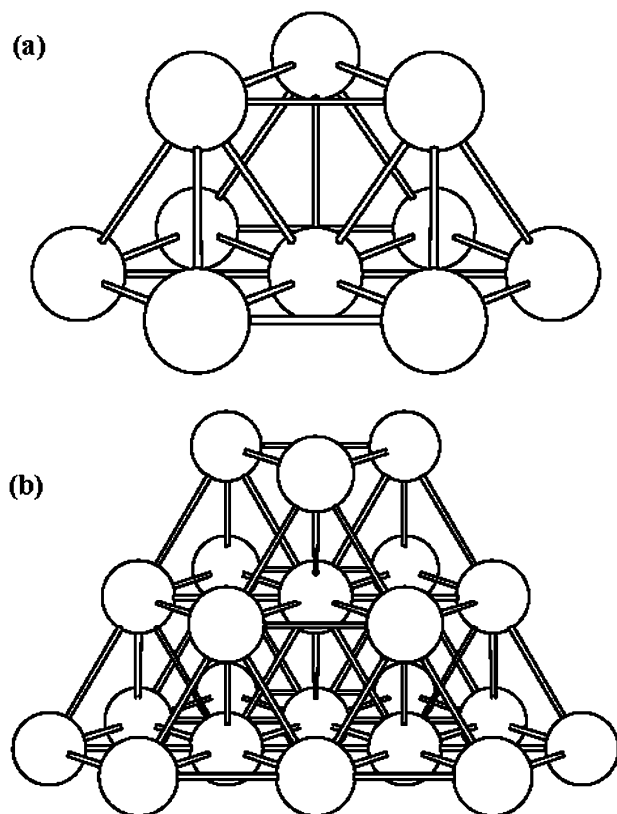


Fig. 6 Structures of (Au)₁₀ (a) and (Au)₂₂ (b) model clusters used for the DFT calculations.

than the flat terrace sites, a popular Au₁₀ cluster is used upset to represent a defect site (Fig. 6a). To examine the size dependency, a larger Au₂₂ cluster is made by adding twelve Au atoms as a third layer to the upset Au₁₀ cluster (Fig. 6b). Fig. 7A shows the n -dependence of μ in vacuum for (Au)₁₀ (a) and

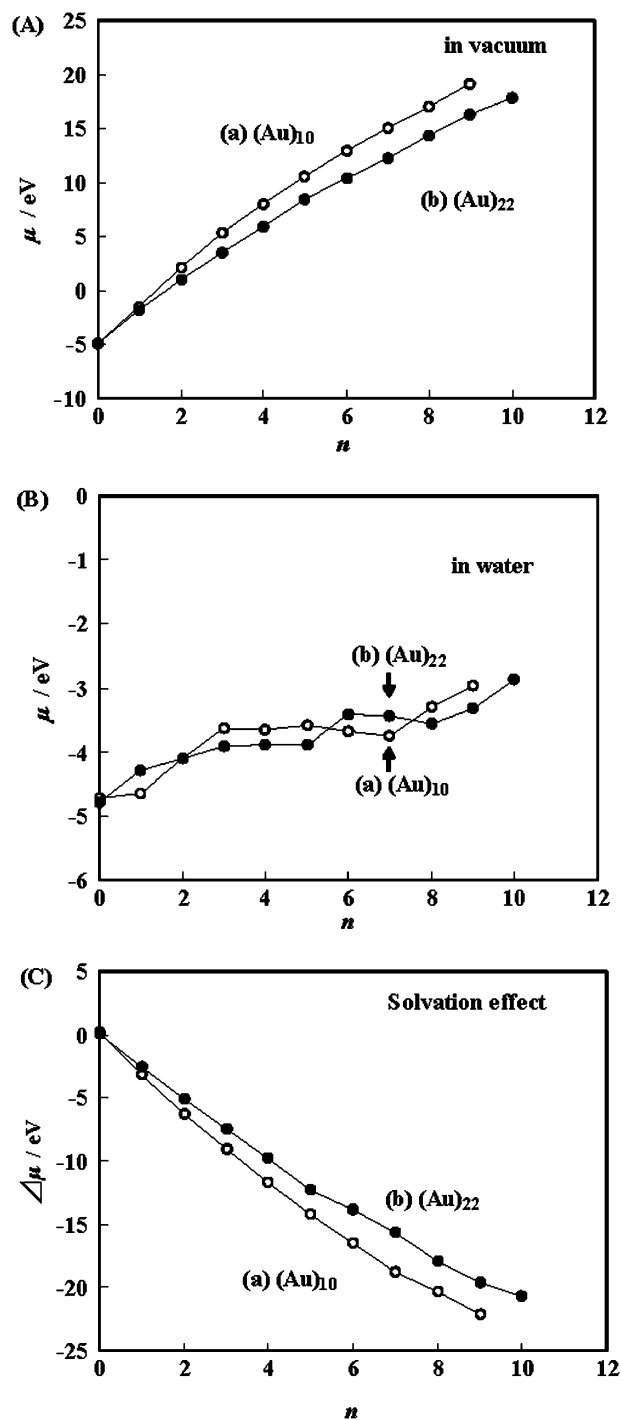


Fig. 7 (A) Plots of the μ value for the Au clusters calculated in vacuum as a function of the number of excess electrons (n): (a) (Au)₁₀, (b) (Au)₂₂. (B) Plots of the μ value calculated in water by the PCM model as a function of n : (a) (Au)₁₀, (b) (Au)₂₂. (C) Difference in the μ value between in vacuum and in water as a function of n : (a) (Au)₁₀, (b) (Au)₂₂.

(Au)₂₂ (b). In each system, the μ value steeply increases with an increase in n , and the increment of μ for (Au)₁₀ is larger than that for (Au)₂₂ at the same n . Recently, the research group of Kamat has prepared Au(3 < d < 8 nm)/TiO₂ particles using 3-mercaptopropionic acid (3-MPA) as a bifunctional coupling agent, measuring the Fermi energy of Au/TiO₂ in a toluene-ethanol mixed solvent using C₆₀/C₆₀[−] as a redox pair.⁴³ As a result, they observed a trend opposite to ours that the E_F' increases with decreasing d , attributing this to the quantum size effect of Au NPs. Clearly, the change in μ in Fig. 7A is overestimated; however, the trend is in agreement with that reported by Kamat *et al.* Also, the research group of Goodman has revealed using scanning tunneling microscopy/spectroscopy that an Au particle formed on the surface of a TiO₂ single crystal undergoes metal-to-nonmetal transformation when its dimension is smaller than 3.5 nm in diameter \times 1.0 nm in height.⁴⁴ Therefore, in low polar solvents such as a toluene-ethanol mixed solvent (relative dielectric constant, $\epsilon_r = 13.8$), the μ value for the same n would increase with decreasing d because of the increase in the gap of adjacent energy levels. Fig. 7B shows the μ value calculated with the PCM taking the solvent effect by water as a function of n for (Au)₁₀ (a) and (Au)₂₂ (b). The μ value for each cluster in water is close to that in vacuum at $n = 0$, increasing with increasing n ; however, the increment significantly decreases to be exactly comparable with the experimental data (Fig. 3B). These findings indicate that charged Au NPs are greatly stabilized in water by the solvation. Consequently, the difference in μ between (Au)₁₀ and (Au)₂₂ becomes small and the magnitudes of μ are even interchanged in an irregular way. Fig. 7C shows the difference in μ between in vacuum and in water ($\Delta\mu = \mu(\text{water}) - \mu(\text{vacuum})$) for (Au)₁₀ (a) and (Au)₂₂ (b). The fact that (Au)₁₀ ^{n^-} clusters are more stabilized than (Au)₂₂ ^{n^-} clusters is consistent with the higher charge density per Au atom for (Au)₁₀ ^{n^-} , pointing out the important contribution of the solvation energy to the E_F' in water ($\epsilon_r = 80.1$). Unexpectedly, the E_F' for the Au/TiO₂ in a toluene-ethanol solution⁴³ is lower than that determined by in water by *ca.* 0.2 eV. A possible explanation is that 3-MPA used as a coupling agent suppresses the interfacial electron transfer because an insulating layer with thickness of only 0.2 nm acts as a significant barrier.⁴⁵ Thus, we concluded that a predominant factor for determining E_F' is the solvation of charged metal NPs and their quantum size effect in polar media and in low polar media, respectively, and the increase in E_F' with increasing d in water arises from the increase in the efficiency of the electron transfer from TiO₂ to Au and the relative decrease in the stabilization energy due to water solvation.

4. Conclusions

The Fermi energy of Au NPs directly coupled with TiO₂ at the photostationary state (E_F') has been determined by the use of S/S^{2−} having a specific interaction with Au as a redox probe. The E_F' in water increases as the mean size of Au NPs (d) increases at 3.0 $\leq d \leq$ 13 nm. The photocatalytic activities of Au/TiO₂-photocatalyzed reductions increase and the TiO₂-PL intensities of Au/TiO₂ decrease with increasing d in parallel with E_F' . These results support the conclusion, which could be

further accounted for in terms of both the increase in the efficiency of the photoinduced electron transfer from TiO₂ to Au and the decrease in the stabilization of charged Au NPs by water solvation. This method is applicable to various metal-semiconductor coupling systems, providing important information on the design of metal NP-loaded semiconductor photocatalytic reactions.

Acknowledgements

This work was partially supported by a Grant-in-Aid for Scientific Research (C) No. 16550169 and (B) No. 20350097 from the Ministry of Education, Science, Sport, and Culture, Japan.

References

- 1 M. Jin, X. Zhang, S. Nishimoto, Z. Liu, D. A. Tryk, A. V. Emeline, T. Murakami and A. Fujishima, *J. Phys. Chem. C*, 2007, **111**, 658, and the references therein.
- 2 K. Rajeshwar, N. R. De Tacconi and C. R. Chenthamarakshan, *Chem. Mater.*, 2001, **13**, 2765, and the references therein.
- 3 V. Subramanian, E. Wolf and P. V. Kamat, *J. Phys. Chem. B*, 2001, **105**, 11439.
- 4 A. Wood, M. Giersig and P. Mulvaney, *J. Phys. Chem. B*, 2001, **105**, 8810.
- 5 K. Hashimoto, H. Irie and A. Fujishima, *Jpn. J. Appl. Phys.*, 2005, **44**, 8269.
- 6 H. Li, Z. Bian, J. Zhu, Y. Huo, H. Li and Y. Lu, *J. Am. Chem. Soc.*, 2007, **129**, 4538.
- 7 G. Palmisano, V. Augugliaro, M. Pagliaro and L. Palmisano, *Chem. Commun.*, 2007, 3425.
- 8 H. Tada, K. Teranishi, Y. -i. Inubushi and S. Ito, *Chem. Commun.*, 1998, 2345.
- 9 H. Tada, F. Suzuki, S. Yoneda, S. Ito and H. Kobayashi, *Phys. Chem. Chem. Phys.*, 2001, **3**, 1376.
- 10 H. Tada, T. Ishida, A. Takao, S. Ito, S. Mukhopadhyay, T. Akita, K. Tanaka and H. Kobayashi, *ChemPhysChem*, 2005, **6**, 1537.
- 11 H. Tada, T. Ishida, A. Takao and S. Ito, *Langmuir*, 2004, **20**, 7898.
- 12 D. Cahen, G. Hodes, M. Graetzel, J. F. Guillemoles and I. Riess, *J. Phys. Chem. B*, 2000, **104**, 2053.
- 13 Y. Nakato, M. Shioji and H. Tsubomura, *Chem. Phys. Lett.*, 1982, **90**, 453.
- 14 M. Jakob, H. Levanon and P. V. Kamat, *Nano Lett.*, 2003, **3**, 353.
- 15 H. Tada, T. Soejima, S. Ito and H. Kobayashi, *J. Am. Chem. Soc.*, 2004, **126**, 15952.
- 16 S. Tsubota, M. Haruta, T. Kobayashi, A. Ueda and Y. Nakahara, *Preparation of Catalysis V*, Elsevier, Amsterdam, 1991.
- 17 M. J. Frisch, G. W. Trucks, H. B. Schlegel, G. E. Scuseria, M. A. Robb, J. R. Cheeseman, V. G. Zakrzewski, J. A. Montgomery, Jr, R. E. Stratmann, J. C. Burant, S. Dapprich, J. M. Millam, A. D. Daniels, K. N. Kudin, M. C. Strain, O. Farkas, J. Tomasi, V. Barone, M. Cossi, R. Cammi, B. Mennucci, C. Pomelli, C. Adamo, S. Clifford, J. Ochterski, G. A. Petersson, P. Y. Ayala, Q. Cui, K. Morokuma, D. K. Malick, A. D. Rabuck, K. Raghavachari, J. B. Foresman, J. Cioslowski, J. V. Ortiz, B. B. Stefanov, G. Liu, A. Liashenko, P. Piskorz, I. Komaromi, R. Gomperts, R. L. Martin, D. J. Fox, T. Keith, M. A. Al-Laham, C. Y. Peng, A. Nanayakkara, C. Gonzalez, M. Challacombe, P. M. W. Gill, B. Johnson, W. Chen, M. W. Wong, J. L. Andres, C. Gonzalez, M. Head-Gordon, E. S. Replogle and J. A. Pople, *GAUSSIAN 98 (Revision A5)*, Gaussian Inc., Pittsburgh, PA, 1998.
- 18 (a) A. D. Becke, *J. Chem. Phys.*, 1993, **98**, 1372; (b) A. D. Becke, *J. Chem. Phys.*, 1993, **98**, 5648.
- 19 P. M. W. Gill, B. G. Johnson and J. A. Pople, *Int. J. Quantum Chem. Symp.*, 1992, **26**, 319.
- 20 A. D. Becke, *Phys. Rev. A*, 1988, **38**, 3098.
- 21 C. Lee, W. Yang and R. G. Parr, *Phys. Rev. B*, 1988, **37**, 785.
- 22 P. J. Hay and W. R. Wadt, *J. Chem. Phys.*, 1985, **82**, 270; P. J. Hay and W. R. Wadt, *J. Chem. Phys.*, 1985, **82**, 299.

- 23 T. H. J. Dunning and P. J. Hay, in *Modern Theoretical Chemistry*, ed. H. F. Schaefer III, Plenum Press, New York, 1976, pp. 1–35.
- 24 S. Miertus, E. Scrocco and J. Tomasi, *Chem. Phys.*, 1981, **55**, 117.
- 25 H. Tada and H. Honda, *J. Electrochem. Soc.*, 1995, **142**, 3438.
- 26 H. Tada, K. Teranishi, Y.-i. Inubushi and S. Ito, *Langmuir*, 2000, **16**, 3304.
- 27 T. Kiyonaga, T. Mitsui, M. Torikoshi, M. Takekawa, T. Soejima and H. Tada, *J. Phys. Chem. B*, 2006, **110**, 10771.
- 28 H. Gerischer and A. Heller, *J. Electrochem. Soc.*, 1992, **139**, 113.
- 29 C. Vricat, M. E. Vela, G. Andreassen and R. C. Salvarezza, *Langmuir*, 2001, **17**, 4919.
- 30 T. Kiyonaga, T. Mitsui, T. Soejima, S. Ito, H. Tada, T. Kawahara, T. Akita, K. Tanaka and H. Kobayashi, *ChemPhysChem*, 2005, **6**, 2508.
- 31 S. Miyazaki, T. Kiyonaga, T. Kawahara and H. Tada, *Chem. Lett.*, 2007, **36**, 1214.
- 32 A. N. Buckley, I. C. Hamilton and R. Woods, *J. Electroanal. Chem.*, 1987, **216**, 213.
- 33 C. Vricat, G. Andreassen, M. E. Vela and R. C. Salvarezza, *J. Phys. Chem. B*, 2000, **104**, 302.
- 34 T. Kiyonaga, T. Kawahara and H. Tada, *Electrochem. Solid-State Lett.*, 2006, **9**, E9.
- 35 A. J. Bard and L. R. Faulkner, *Electrochemical Methods Fundamentals and Applications*, John Wiley & Sons, Inc., New York, 2nd edn., 2001.
- 36 L. Yang, W. Fu, H. Fu and J. Sun, *Sol. Energy Mater. Sol. Cells*, 2006, **90**, 1773.
- 37 U. Kreibig and M. Vollmer, *Optical Properties of Metal Clusters.*, Springer, Berlin, 1995.
- 38 D. Li, H. Haneda, S. Hishhita, N. Ohashi and N. K. Labhsetwar, *J. Fluorine Chem.*, 2005, **126**, 69.
- 39 B. Xin, L. Jing, Z. Ren, B. Wang and H. Fu, *J. Phys. Chem. B*, 2005, **109**, 2805.
- 40 A. Furube, T. Asahi, H. Masuhara, H. Yamashita and M. Anpo, *J. Phys. Chem.*, 1999, **103**, 3120.
- 41 J. S. Curran, J. Domenech, N. Jaffrezic-Renault and R. Phillippe, *J. Phys. Chem.*, 1985, **89**, 957.
- 42 Y. Nosaka, Y. Ishizuka and H. Miyama, *Ber. Bunsen-Ges. Phys. Chem.*, 1986, **90**, 1199.
- 43 V. Subramanian, E. E. Wolf and P. V. Kamat, *J. Am. Chem. Soc.*, 2004, **126**, 4943.
- 44 M. Valden, X. Lai and D. W. Goodman, *Science*, 1998, **281**, 1647.
- 45 N. Mukaihata, H. Matsui, T. Kawahara, H. Fukui and H. Tada, *J. Phys. Chem. C*, 2008, **112**, 8702.